AIAA JOURNAL
Vol. 48, No. 1, January 2010

Flame Stabilization in Small Cavities

Alejandro M. Briones*
University of Dayton Research Institute, Dayton, Ohio 45469
Joseph Zelina†
U.S. Air Force Research Laboratory, Wright-Patterson Air Force Base, Ohio 45433
and
Viswanath R. Katta‡
Innovative Scientific Solutions, Inc., Dayton, Ohio 45440

DOI: 10.2514/1.44162

This research is motivated by the necessity to improve the performance of ultracompact combustors, which requires flame stabilization in small cavities. An extensive computational investigation on the characteristics of cavity-stabilized flames is presented. A high-fidelity, time-accurate, implicit algorithm that uses a global chemical mechanism for JP8-air combustion and includes detailed thermodynamic and transport properties as well as radiation effects is used for simulation. Calculations are performed using both direct numerical simulation and standard k-ε Reynolds-averaged Navier–Stokes model. The flow unsteadiness is first examined in large axisymmetric and small planar cavities with nonreactive flows. As with previous investigations on axisymmetric cavities, multiple flow regimes were obtained by varying cavity length (x/D_o): wake backflow regime, unsteady cavity vortex regime, steady cavity vortex regime, and compressed cavity vortex regime. However, planar cavities only exhibit steady cavity vortex and compressed cavity vortex regimes. Two opposed nonaligned air jets were positioned in this planar cavity: the outermost air jet in coflow with the mainstream flow (i.e., normal injection). The fuel jet was injected either in coflow, crossflow, or counterflow with respect to the mainstream flow. Flow unsteadiness was observed to be relatively small for coflow- and crossflow-fuel-jet injection. By reversing the air jet positions (i.e., reverse injection), the flow unsteadiness is promoted regardless of fuel jet positioning. Finally, the effect of combustion and cavity equivalence ratio (ϕ_{CAV}) on flame unsteadiness is addressed. With normal injection (reverse injection), low and high ϕ_{CAV} leads to low (high) and high (low) flame unsteadiness, respectively. Based on these results recommendations are provided to designers/engineers to reduce flame unsteadiness in these cavities.

Nomenclature

C_P	=	pressure coefficient
D	=	planar cavity depth
D_o	=	forebody diameter
D_S	=	spindle diameter
L	=	planar cavity length
Re_D	=	global Reynolds number based on cavity depth, D
Re_x	=	cavity Reynolds number based on axisymmetric cavity length, x
R_o	=	forebody radius
x	=	axisymmetric cavity length
ΔC_D	=	change in drag
$\Delta C_{D,P}$	=	change in pressure drag
$\Delta C_{D,S}$	=	change in shear drag
λ_{CAV}	=	cavity air to fuel jet momentum ratio
ϕ_{CAV}	=	cavity equivalence ratio

I. Introduction

MAJOR advances in combustor technology are required to meet the conflicting challenges of improving performance, increasing durability, reducing weight, lowering emissions, and maintaining cost. A novel approach proposed by the U.S. Air Force Research Laboratory/RZTC [1,2] is the development of the ultracompact combustor (UCC). The UCC design uses high swirl in a circumferential cavity (cavity refers to a space lacking of solid and filled with gas) to enhance mixing rates via high cavity gravity loading on the order of $3000g$. The UCC shows how the primary, intermediate, and dilution zones of a conventional combustor can be incorporated into a much smaller footprint using compressor and turbine features that enable a shorter and potentially less complex gas turbine. It combines the high-gravity combustor circumferential cavity and strut with the compressor exit vanes and the high-pressure turbine inlet guide vanes (IGV). Because recent investigations [3] on the UCC have shown promising improvements on performance for future engine implementation, it is envisioned that the UCC could be either used as the main combustor or as an interturbine burner between the high- and low-pressure turbines to operate in a reheat cycle engine.

A schematic of the current UCC is shown in Fig. 1. The main air (or vitiated) flow enters the combustor and flows around the bullet nose of the center body. The turning vanes (indicated as "guide vane") simulate the swirl that would be coming from the compressor rotor in a real gas turbine engine. The flow from the trailing edge of these turning vanes impinges on the IGV (indicated as "blade"). The function of the IGV is the same as that of a conventional gas turbine engine. A radial cavity located in the IGV, aligned with the circumferential cavity, facilitates transport of gases from the circumferential cavity to the main stream. Additional air is admitted through 24 holes equally spaced around the circumferential cavity and angled at 45 deg to the radial direction to promote high swirl in the cavity. At the cavity-in-cavity (CIC), a small amount of air is injected and fuel is sprayed into the circumferential cavity. This allows fuel-rich combustion to occur in the circumferential cavity. Consequently, combustion primarily takes place in the engine circumferential direction rather than in the axial direction as is conventionally done. The circumferential cavity is analogous to a centrifuge; hence, cold nonreactive fuel–air mixture migrates radially outward, whereas hot

Received 5 March 2009; revision received 5 August 2009; accepted for publication 10 August 2009.

*Research Engineer, Energy and Environmental Engineering Division, 300 College Park/0043. Member AIAA.
†Senior Research Engineer, 1950 Fifth Street. Associate Fellow AIAA.
‡Senior Research Engineer, 2766 Indian Ripple Road. Senior Member AIAA.

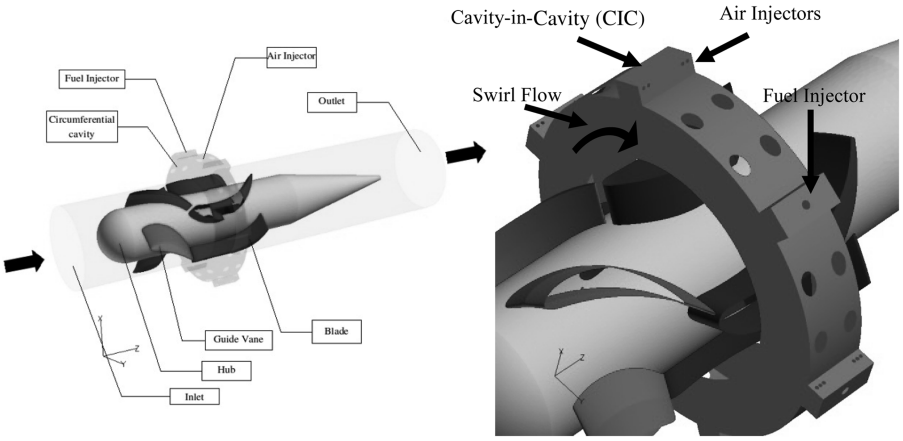

Fig. 1 Ultracompact combustor; inlet, hub, guide vane, blade, circumferential cavity, outlet, cavity-in-cavity, air injectors, and fuel injectors are indicated. The swirl flow is also indicated by the bent arrow on the circumferential cavity.

reacted mixture migrates radially inward. The cold mixture remains in the circumferential cavity for a longer period of time to evaporate, mix, and burn. The large density gradient in the cavity along with the high-gravity flow enhances mixing of cold and hot mixtures creating a very well-mixed combustion zone. The intermediate products of combustion are transported by lower wake pressures into the radial cavities where fuel-lean combustion occurs.

Numerous design variations of the selected configurations have been evaluated, leading to improved configurations with optimized performance and higher efficiency [3–7]. Although the UCC exhibits many advantageous features over conventional burners, it poses a particular difficulty regarding lean blowout and flame stability. The CIC shown in Fig. 1 was one of the latest additions to the UCC. Without the CIC, the gaseous flow high speed and acceleration in the circumferential cavity demands fuel injection with low residence times. In addition, the high-gravity loading enhances strain rates and, consequently, promotes extinction. The CIC is a workaround to these problems by channeling a second cavity inside the primary one. The fuel injected with additional air jets through the CIC is to increase fuel-injection residence times and to reduce local strain rates, while enhancing the fuel-air mixing. Hence, the small CIC with dimensions of a few millimeters and inherent global Reynolds number $Re_D \approx 10,000$ acts as a flame holder. [We refer to small cavities as those whose dimensions are very small in comparison with the characteristic length of the combustor. For instance, our planar cavity exhibits cavity length to combustor length of $\sim$10% (cf. Fig. 1). It turns out that these cavities generally exhibit global Reynolds number $(Re_D) \approx 10,000$. On the other hand, we refer to large cavities as those with cavity length to combustor length greater than $\sim$50% with usual Re_D greater than 10,000 (e.g., $(Re_D) \approx 70,000$). Large cavities reported in the literature usually exhibit one order of magnitude larger residence time than small cavities.] Even though the CIC concept has proven to enhance the performance of the UCC, there is still further need for improvement [3]. The fuel and air jets in the CIC create vortices, which, depending on the cavity dimensions, equivalence ratio, and injector positions, could lead to highly unstable flow. This in turn leads to flame instability, which induces higher residence times and promotes fuel-rich environments that increase pollution and soot formation. Therefore, current efforts are oriented toward determining design criteria for reducing flame fluctuations in the CIC.

Most previous investigations have dealt with nonreactive and reactive flow stability criteria in large axisymmetric [8–11] and planar [12–15] cavities with dimensions on the order of a few centimeters, $Re_D > 10,000$, and an order of magnitude larger residence time than those expected in the CIC.[§] Consequently, the flow/flame stabilization in the CIC is more complicated than in previous studies [8–15]. For instance, for large cavities, the fuel is nearly fully consumed inside the cavity and the flame is contained in the cavity [10,11,15]. On the contrary, in CIC-like cavities, very little amount of the fuel is burned in the cavity, extending the flame outside it [16]. Despite these facts, it is worth discussing the flow/flame stabilization criteria in large cavities because it provides insights into flame stabilization in CIC-like cavities. Mair [8] experimentally examined the effect of an afterbody disk on the drag of a blunt-based forebody-spindle object. His experiments showed that the drag of the forebody-spindle object is significantly reduced by mounting an afterbody disk. Further reduction in drag was observed by mounting a secondary afterbody disk. Little and Whipkey [9] performed similar experiments. They identified three regimes associated with drag. These are the wake backflow (WBF), unsteady cavity vortex (UCV), and the steady cavity vortex (SCV) regime. In the WBF, flow downstream the afterbody spills upstream into the cavity and the cavity exhibits a counter-rotating vortex[¶] with high-drag coefficient. By moving the afterbody disk downstream from where WBF regime exists, the flow in the cavity transitions to the UCV regime. The cavity exhibits a corotating vortex[**] and the wake backflow does not move upstream past the afterbody disk. The drag coefficient C_D fluctuates from low- to high-drag condition. When the disk is positioned at its optimum from the forebody, the flow in the cavity is said to be in the SCV regime. Here, the vortex rotates (with edge velocity) in the same direction as the mainstream velocity, fits the cavity nearly perfectly, mass transfer into or out of the cavity is minimum, there is no backflow, and is characterized by low drag. Their cavity optimization criterion was based so that, to reduce C_D, the afterbody disk needs to be large enough to separate the wake backflow from the cavity flow so that a locked vortex can exist in the cavity. Therefore, with the proper choice of cavity dimensions, vortices in the cavity can be made stationary. However, a steady vortex yields minimum mass exchange between the vortex and the main flow, which in the CIC means that additional air must be supplied within the cavity for combustion to be sustainable. Consequently, Katta and Roquemore [10,11] conducted an extensive numerical investigation to determine the effect of combustion on cavity-stabilized flames. They showed that, for nonreactive flow, both standard k-ε Reynolds-averaged Navier–Stokes (RANS) model and direct numerical simulation (DNS) can be used to predict ΔC_D with cavity size. They also showed that the optimum cavity length determined from nonreactive flows yields to nonshedding cavity flows, even with combustion and primary injection into the cavities.

Planar cavities better emulate the shape of the CIC (cf. Figure 1). Zdanski et al. [12,13] numerically studied the nonreactive flow past two-dimensional trenchlike cavities and showed that, with increasing

[§]The residence time scales with length for turbulent flows.

[¶]Throughout the text, counter-rotating vortex means that the vortex edge velocity is in the opposed direction to the mainstream velocity. The mainstream flow is not rotating.

[**]Throughout the text, corotating vortex means that the vortex edge velocity is in the same direction as the mainstream velocity. The mainstream flow is not rotating.

Table 1 Transport coefficients and source terms appearing in governing equations

Equations	Φ	Γ^{Φ}	S^{Φ}
Continuity	1	0	0
Axial momentum	u	μ	$-\frac{\partial P}{\partial z}+(\rho_0-\rho)g+\frac{\partial}{\partial z}\left(\mu\frac{\partial u}{\partial z}\right)+\frac{\partial}{\partial r}\left(\mu\frac{\partial v}{\partial z}\right)+\frac{\mu}{r}\frac{\partial v}{\partial z}-\frac{2}{3}\left\{\frac{\partial}{\partial z}\left(\mu\frac{\partial u}{\partial z}\right)+\frac{\partial}{\partial z}\left(\mu\frac{\partial v}{\partial r}\right)\right\}+\frac{\partial}{\partial z}\left(\mu\frac{v}{r}\right)$
Radial (transverse) momentum	v	μ	$-\frac{\partial P}{\partial r}+\frac{\partial}{\partial r}\left(\mu\frac{\partial u}{\partial r}\right)+\frac{\partial}{\partial r}\left(\mu\frac{\partial v}{\partial r}\right)+\frac{\mu}{r}\frac{\partial v}{\partial r}-2\mu\frac{v}{r^2}-\frac{2}{3}\left\{\frac{\partial}{\partial r}\left(\mu\frac{\partial u}{\partial z}\right)+\frac{\partial}{\partial r}\left(\mu\frac{\partial v}{\partial r}\right)\right\}+\frac{\partial}{\partial r}\left(\mu\frac{v}{r}\right)$
Species mass fraction	Y_i	$\rho D_{i-\mathrm{mix}}$	$\dot{\omega}_i$
Energy	H	$\frac{\lambda}{c_p}$	$\nabla\left[\frac{\lambda}{c_p}\sum_1^{N_S}\left\{\left(Le_i^{-1}-1\right)H_i\nabla Y_i\right\}\right]-\sum_1^{N_S}\left\{h_{f,i}^0\dot{\omega}_i\right\}+q_{\mathrm{rad}}$

the cavity aspect ratio, two vortices in the cavity appear. At a critical aspect ratio, the external flow reattaches to the surface that is parallel to the mainstream flow. Similarly, D'yanchenko et al. [14] experimentally studied the nonreactive flow past heated two-dimensional trenchlike cavities with inclined frontal and rear walls. They showed that, for an interval of wall inclination angles, the flow in the cavity becomes unstable with the primary vortex changing its structure from single cellular to double cellular. Recently, Puranam et al. [15] investigated experimentally the flame stabilization in a curving, contracting channel with an inner large cavity. They showed that, at low Reynolds number (1000–10,000), the flame extends outside the cavity, whereas at high Reynolds number ($\geq 40,000$), combustion occurs inside the cavity. In between these regimes, the flame was unstable.

Because flow/flame stabilization in small cavities is so specialized, there are (to the best of our knowledge) only two investigations reported in the literature. Zelina et al. [3] experimentally studied multiple air injection strategies on the performance of the CIC, while the fuel was injected radially as in Fig. 1. The configurations included the following: (config. 1) two-nonaligned opposed air jets with the outermost jet in coflow with the mainstream flow, (config. 2) one single innermost air jet in counterflow with the mainstream flow, and (config. 3) no air jets. Cavity equivalence ratio ϕ_{CAV} at lean blowout was found to be as low as 0.08 for config. 3 and as high as 1.5 for config. 1. Decreasing the cavity air to fuel momentum ratio λ_{CAV} led to higher ϕ_{CAV} at lean blowout for all configurations. Moreover, Katta et al. [16] performed two-dimensional, unsteady, reacting flow numerical simulations on a trenchlike cavity with fuel and air injections. The parametric investigation indicated that there is a cavity optimum size that minimizes flow unsteadiness. Therefore, the purpose of this investigation is to enhance our understanding regarding cavity-stabilized flames that might lead to the development of concepts for the design of higher performance CIC. First, we will start by reviewing and expanding the discussion on the criteria of flow unsteadiness in large axisymmetric cavities. Second, we will apply the concepts related to large axisymmetric cavities to small planar cavities. Third, the effect of fuel and air injections on flow unsteadiness will be addressed for small planar cavities. Fourth, the effect of fuel-injection positioning to flow unsteadiness will be examined in small planar cavities. Then, the effect of air injection positioning on flow unsteadiness will also be investigated in these cavities. Finally, we will discuss the effect of combustion and cavity equivalence ratio on flow/flame unsteadiness.

II. Physical-Numerical Procedure

A. Gas-Phase Numerical Model

The numerical model is based on the solution of the time-dependent governing equations for a two-dimensional unsteady reacting flow [17,18]. Using cylindrical coordinates (r, z) these equations can be written as

$$\frac{\partial(\rho\Phi)}{\partial t}+\frac{\partial(\rho v\Phi)}{\partial r}+\frac{\partial(\rho u\Phi)}{\partial z}=\frac{\partial}{\partial r}\left(\Gamma^{\Phi}\frac{\partial\Phi}{\partial r}\right)+\frac{\partial}{\partial z}\left(\Gamma^{\Phi}\frac{\partial\Phi}{\partial z}\right)-\frac{\rho v\Phi}{r}+\frac{\Gamma^{\Phi}}{r}\frac{\partial\Phi}{\partial r}+S^{\Phi} \tag{1}$$

Here, t denotes the time, ρ the density, and u and v the axial z and radial r velocity components, respectively. The general form of the equation represents conservation of mass, momentum, species, or energy conservation, depending on the variable used for Φ. The diffusive transport coefficient Γ^{Φ} and source terms S^{Φ} are described in Table 1. Introducing the overall species conservation equation and the state equation completes the equation set. In addition, a sink term based on an optically thin gas assumption is included in the energy equation to account for thermal radiation from the flame [19]. The sink term due to the radiation heat loss is expressed as $q_{\mathrm{rad}}=-4\sigma K_p(T^4-T_o^4)$ [20] where T denotes the local flame temperature. The term K_p accounts for the absorption and emission from the participating gaseous species (CO_2, H_2O, CO, and CH_4) and is expressed as

$$K_p=P\sum_k X_i K_{p,i}$$

where $K_{p,i}$ denotes the mean absorption coefficient of the kth species. Its value is obtained by using a polynomial approximation to the experimental data provided in [21].

The finite difference forms of the momentum equations are obtained using QUICKEST scheme [22], whereas those of the species and energy are obtained using a hybrid scheme of upwind and central differencing. The pressure field is calculated at every time

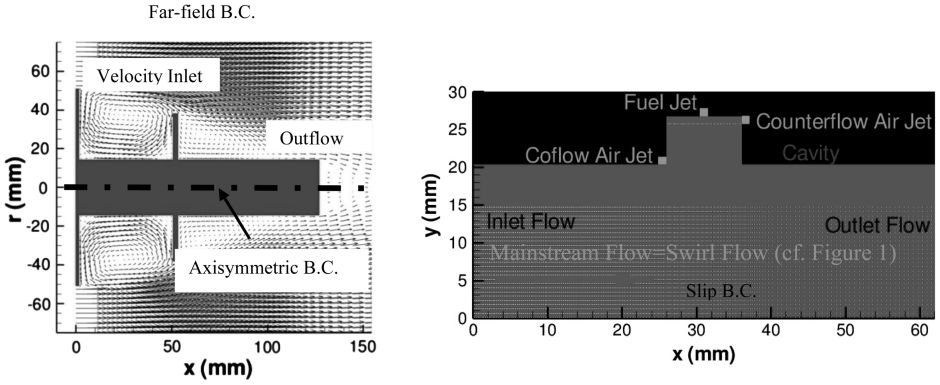

Fig. 2 Computational domains for the axisymmetric cavity (left) and the planar cavity (right). The axisymmetric cavity has been mirrored. The sample axisymmetric cavity corresponds to the case in which the afterbody disk is placed at $x/D_o = 0.5$. The whole computational domain is not shown here. The planar cavity indicates the location of the injections in its normal configuration. The boundary conditions are also indicated. The air mainstream flow direction is also indicated for the small planar cavity case. Note that the air mainstream flow corresponds to the swirl flow in Fig. 1.

step by solving all of the pressure Poisson equations simultaneously and using the lower and upper diagonal matrix-decomposition technique.

Figure 2 illustrates the computational domains for the large axisymmetric and small planar cavities. They consist of 229 × 229 mm and 62 × 30 mm in the axial x and radial r (vertical y) directions, respectively, and are represented by a staggered, nonuniform grid system (300 × 300 and 401 × 421, respectively). The axisymmetric cavity contains a forebody with diameter D_o of 101.6 mm, spindle diameter D_S of 28.6 mm, afterbody disk diameter D_1 of 38.1 mm, afterbody disk thickness of 1.5 mm, and spindle length of 127 mm. The upstream flow approaches the forebody-spindle-afterbody geometry at uniform and constant velocity and temperature of 30.5 m/s and 300 K, respectively. Throughout this investigation, only the distance of the afterbody disk to the forebody is varied. Only nonreactive flow conditions and standard k-ε RANS simulations are performed on the axisymmetric cavities. The planar cavity consists of a forebody and an afterbody of equal depth D. Although the separation distance of the forebody and afterbody is varied in this study, the depth D is maintained constant at 6.4 mm. For nonreactive flow conditions, the air mainstream approaches the cavity at uniform and constant velocity and temperature of 40 m/s and 300 K. Both DNS and RANS simulations and both nonreactive and reactive flow conditions are performed on the planar cavities. Fuel and air injections are also used in planar cavities. The cavity equivalence ratio ϕ_{CAV} is also varied. Additional details are provided in subsequent sections.

B. Thermodynamic and Transport Properties

The thermodynamic and transport properties appearing in the governing equations are temperature and species dependent. The mixture density is computed using the ideal gas law assuming that the pressure remains constant in the flowfield at 101,325 Pa. The specific heat capacity of individual species is computed with piecewise polynomials [10]. The viscosity, thermal conductivity, and binary diffusivity of the individual species were based on kinetic theory [23]. Whereas the mixture viscosity and thermal conductivity are computed using the Wilke semi-empirical formulas [24], mixture-averaged formulation is used to compute species diffusivities that are used in the governing equations. The Wilke semi-empirical correlations are used because they apply to nonpolar low-density gases; hence, these correlations are useful in our investigation. The mixture-averaged diffusivity is a particularly useful simplification when all species, but one, are not abundant. For instance, the mass fraction of N_2 is ~0.72. The formulation used for the calculation of individual and mixture properties is a common practice used in many in-house source codes [25] and commercial codes [26,27].

C. Combustion Model

The JP8-air chemistry is modeled using a global reaction mechanism involving five species, namely JP8, O_2, CO_2, H_2O, and N_2. JP8 is treated as a surrogate mixture consisting of six parent species: 30% n dodecane, 20% n tetradecane, 10% i octane, 20% methylnaphthalene, 5% tetralin, and 15% m xylene [28]. The global reaction for this surrogate mixture is

$$\mathrm{JP\,8} + 15.425\mathrm{O_2} \rightarrow 10.25\mathrm{H_2O} + 10.3\mathrm{CO_2}$$

III. Results and Discussion

A. Validation of Numerical Model

The validation of the numerical model has been presented in a previous investigation by Katta and Roquemore [10]. They compared the change in pressure drag $\Delta C_{D,P}$ as a function of afterbody disk distance from the forebody x/D_o for two spindle sizes. Both results of DNS and standard k-ε RANS models were compared with the measurements of Little and Whipkey [9]. Although their RANS simulations did not result in the dynamic flow observed in the experiments, the drag coefficients compared favorably with those from the experiments. On the contrary, the DNS yielded dynamic flows similar to those observed in the experiments and the drag coefficients were not as favorable with the experiments. For the small and large spindle sizes used in their investigation, the RANS simulations predicted a minimum $\Delta C_{D,P}$ similar to that of the measurements. Moreover, the DNS and RANS algorithms have been extensively validated in many unsteady reacting flow simulations, such as opposed jet flames [29] and buoyant jet diffusion flames [30]. Furthermore, the numerical simulations of the trapped-vortex combustor (TVC) [11], which is similar to our large axisymmetric cavity except that it has fuel and air injections, yielded only qualitative comparison with the experiments in terms of temperature profiles. The DNS results were in closer agreement to the experiments than those obtained with RANS. However, the ability of incorporating standard k-ε RANS model in predicting reacting flows was tested in vertically mounted turbulent jet flames [11]. Good qualitative and quantitative agreements were predicted by both the models. Based on these results and the discrepancies presented in the TVC, it was speculated that the standard k-ε RANS model is only inadequate to predict reacting flows in TVC and in large axisymmetric cavities. Nevertheless, the standard k-ε RANS model can qualitatively obtain general features of large axisymmetric cavities exposed to nonreacting flows as shown in Fig. 2 of [10]. Therefore, in this investigation, the standard k-ε RANS model is used for nonreacting flows, whereas the DNS is used for both nonreacting and reacting flows.

B. Flow Unsteadiness in Large Axisymmetric Cavities

This section is concerned with the drag and flow characteristics of a locked vortex afterbody shapes formed by thin disks spaced along a central spindle. Figure 3 presents the velocity vector flowfields and streamlines for conditions when the afterbody disk is placed at $x/D_o = 0.2$, 0.4, 0.5, and 0.7. Similar simulations were conducted by Katta and Roquemore [10]. In this figure, the upstream flow diverges due to increased cross-sectional area and, consequently, flow separation occurs at the sharp corner of the forebody. The streamwise pressure gradient increases until the flow reattaches to the spindle downstream the afterbody. For $x/D_o = 0.2$, the flow recirculates behind the afterbody disk. This flow spills over the afterbody disk into the cavity and two vortices are formed in the cavity. The innermost vortex is counter-rotating with respect to the direction of the mainstream, whereas the outermost vortex is corotating with the mainstream. There is also a freestanding stagnation point inside the flowfield, indicating the presence of opposed flows. This flow configuration is called the wake backflow regime and the characteristic cavity Reynolds number Re_x is less than 84,000. For $x/D_o = 0.4$, there is still spillover and two vortices within the cavity exist. However, in comparison with the WBF, there are velocity vectors pointing toward the afterbody disk still with the presence of a stagnation point in the flowfield. This contraction around the disk and backflow is responsible for inducing flow oscillations [9] and the flow is said to be in the unsteady cavity vortex regime with Re_x ranging from 84,000 to 105,000. For $x/D_o = 0.5$, there is no longer backflow over the afterbody disk and the stagnation point has moved to the top of the afterbody wall and the vortex fits nearly perfectly in the cavity. The location of the stagnation point is consistent with that reported by Gharib and Roshko [31] for this type of flow. The flow is in the steady cavity vortex regime, exhibiting $Re_x \approx 105,000$. At $x/D_o = 0.7$, the vortex in the cavity becomes elongated, the mainstream impinges on the afterbody disk, and the stagnation point moves to the front of the afterbody wall. This impingement compresses the vortex and the flow becomes unsteady. We named this flow the compressed cavity vortex regime (CCV) and it exhibits $Re_x > 105,000$. Furthermore, the streamlines suggest that the SCV exhibits minimum mass exchange with the mainstream flow, as expected.

Figure 4 presents the change in pressure drag $\Delta C_{D,P}$ coefficient as a function of axial distance x/D_o, resulting from the addition of disk to forebody-spindle geometry, discussed in the context of Fig. 3. Katta and Roquemore [10] presented in their Fig. 2 the total change in drag, whereas we only present the contribution of pressure drag to

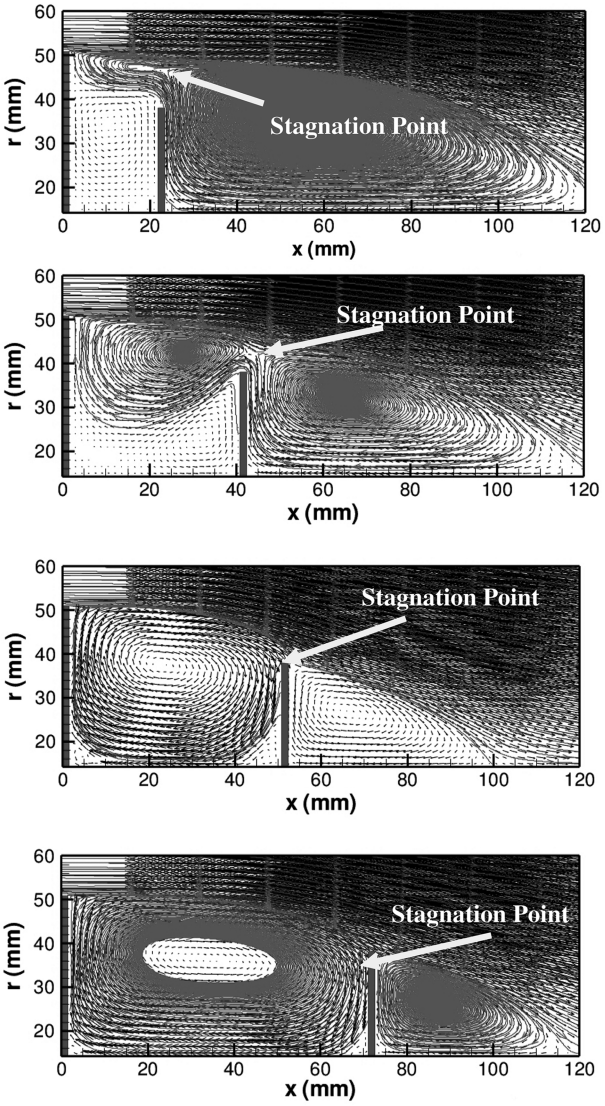

Fig. 3 Velocity vectors for the afterbody disk placed at $x/D_o = 0.2$, 0.4, 0.5, and 0.7. The calculations were performed using the standard k-ε RANS model. The velocity vector lengths are scaled with magnitude. The streamlines are shown. The stagnation points due to reattachment are also indicated.

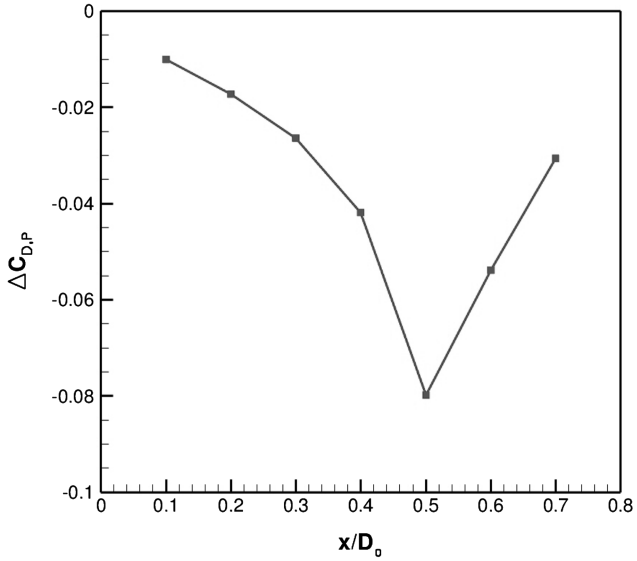

Fig. 4 Change in pressure drag $\Delta C_{D,P}$ coefficient as a function of axial distance x/D_o, resulting from the addition of disk to forebody-spindle geometry. The calculations were performed using the standard k-ε RANS model.

total drag. By comparing our Fig. 4 with Fig. 2 of [10], it is clear that shear drag is nearly negligible. The calculated $\Delta C_{D,P}$ indicates that the drag coefficient decreases monotonically to a minimum value at $x/D_o = 0.5$ and then increases for x/D_o greater than 0.6. Momentum balance on the cavity provides the drag force expressed in terms of the direct forces on the cavity walls or in term of integrated turbulent momentum flux out of the cavity [31]. This momentum flux is inherently unsteady. Increase on the momentum flux indicates increase on flow unsteadiness and thereby increase on drag and drag coefficient (i.e., increase on unbalance forces in the cavity walls). Consequently, the large pressure drag exhibited by the WBF yields oscillations. Similarly, UCV and CCV exhibits larger pressure drags than SCV and these regimes are more unsteady. The flow structure that reduces oscillations is that depicted in Fig. 3 for $x/D_o = 0.5$. Now, in the subsequent paragraph, we relate the minimum $\Delta C_{D,P}$ to the pressure distribution on the forebody face and the upstream face of the afterbody disk.

Figure 5 presents the pressure coefficient C_P as a function of radial coordinate r/R_o at the forebody. The local minima represent the projections of the centers of the vortices on the walls. For the forebody spindle alone without disk, C_P slightly increases from the spindle edge until it reaches an absolute maximum. Further outwardly C_P decreases until it reaches an absolute minimum, indicating the radial location of the center of the vortex. From the center of this vortex, C_P increases to either side at a rate proportional $\sim(r/R_o)^n$, where n is $-1 \leq n \leq 1$. This indicates that this is a freelike vortex structure. When the disk is added at $x/D_o = 0.2$, C_P decreases drastically, suggesting that velocity magnitude increases. However, the C_p distribution is nearly flat with an increase in the outermost edge and a slight increase near the spindle edge. This indicates that velocity magnitudes and circulations corresponding to the outermost corotating and the innermost counter-rotating vortices are comparable, as shown in Fig. 3. Further increase in x/D_o decreases C_p until it reaches a minimum at $x/D_o = 0.5$. When the disk is at this position, the C_P distribution is no longer flat. First, C_p decreases to a local minimum and then it increases to an absolute maximum. This section of the profile indicates the location of a small vortex near the corner of the cavity, as shown in Fig. 3. Further outwardly C_p decreases to an absolute minimum and then rises. This section indicates the existence of a larger vortex in the cavity. In contrast to $x/D_o < 0.5$, the two vortices indicated by the C_p profile suggest that these vortices are forcedlike vortex. This statement is reached because from the center of the vortices C_P now increases with the square of the radius [i.e., $\sim(r/R_o)^2$], which is characteristic of forced vortices. From Fig. 3, note that the velocity magnitude has increased from $x/D_o = 0.2$ to 0.5 as indicated by the length of the velocity vectors. When the disk is positioned further downstream at $x/D_0 = 0.6$, C_p increases again. By positioning the disk even further downstream, C_p increases monotonically with the same qualitative radial distribution as for when the disk was positioned at $x/D_o = 0.5$ and 0.6 (i.e., $n = 2$). The increase in C_p is associated with decrease in velocity magnitudes in the cavity (as indicated by velocity vector lengths in Fig. 3). It is important to point out that the minimum $\Delta C_{D,P}$, which is associated with steady flow, is also associated with minimum C_P on the forebody face. This is in contradiction with the results of Mair [8] which suggested exactly the opposite (i.e., minimum C_P yields maximum $\Delta C_{D,P}$). We believe that the minimum C_P yields minimum $\Delta C_{D,P}$ since $\Delta C_{D,P} = (1/A) \cdot \int C_P \cdot \mathrm{d}A$, where A is the area. In fact, Mair [8] suggested that, in the high-drag regime, the flow was unsteady and the pressures recorded by the manometer may not have been the true mean values. This could have led to data misinterpretation.

Figure 6 presents pressure coefficient C_P as a function of radial coordinate r/R_o at the upstream face of the afterbody disk. At $x/D_o = 0.2$, C_p exhibits a small local minimum near the spindle and then decreases continuously with r/R_o. This indicates that the flow near the disk is moving from the inner regions of the cavity toward

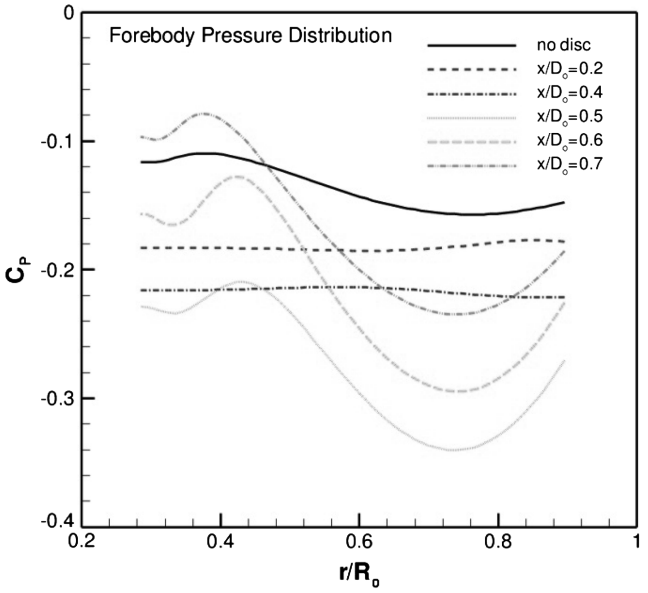

Fig. 5 Pressure coefficient C_P as a function of radial coordinate r/R_o at the forebody. The calculations were performed using the standard k-ε RANS model.

outside (i.e., counter-rotating vortex). With increasing x/D_o to 0.4, the magnitude of C_P decreases and the profile is still nearly similar to that of $x/D_o = 0.2$ because there is still a counter-rotating vortex, as depicted in Fig. 3. Further increase of x/D_o to 0.5 shifts C_P slightly above that of $x/D_o = 0.4$. An absolute minimum C_P is observed to occur. As x/D_o increases to 0.6 and 0.7, the minimum is shifted toward the inside of the cavity. This is due to larger impingement area of the mainstream flow on the afterbody disk, which pushes the vortex toward the spindle. That is why at $x/D_o = 0.6$ and 0.7 the flow is in the CCV regime. According to Zdanski et al. [12,13], if we were to further increase x/D_o, two major vortices would form inside the cavity which depending on x/D_o these vortices could be either encapsulated (i.e., without flow reattachment) or nonencapsulated.

In summary, our results presented from Figs. 3–6 indicate that low flow unsteadiness is achieved when a large corotating vortex with the mainstream, exhibiting forcedlike vortex characteristics, fits the cavity. This leads to low-pressure drag and low-pressure coefficients in both the forebody face and upstream face of the afterbody. RANS simulations are sufficient for determining flow configuration exhibiting low flow unsteadiness.

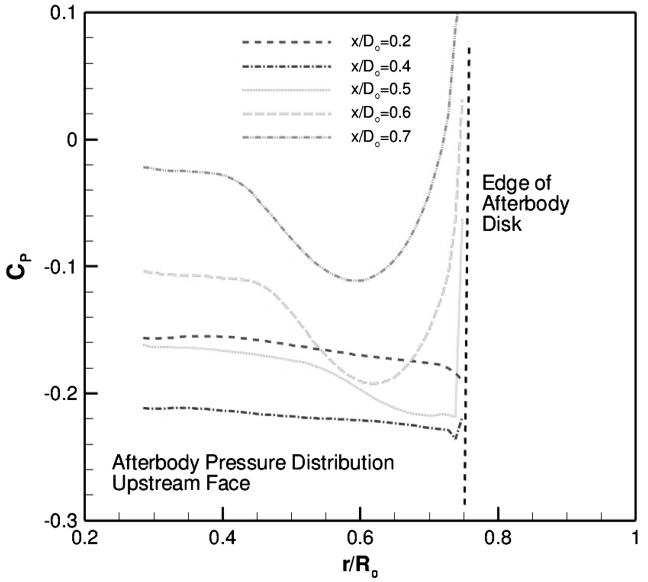

Fig. 6 Pressure coefficient C_P as a function of radial coordinate r/R_o at the upstream face of the afterbody disk. The calculations were performed using the standard k-ε RANS model.

C. Flow Unsteadiness in Small Planar Cavities

From Fig. 1, it is noticed that the CIC has two major geometrical differences with the large axisymmetric cavities studied in the previous section. In the CIC, the thickness of the afterbody is infinitely long and the heights of the afterbody and forebody walls are equal. Therefore, the CIC is modeled as the small planar cavity shown in Fig. 2. Based on the results from the previous section, we expect the wake spillover to be nonexistent, and, consequently, WBF and UCV regimes will be nonexistent as well.

Figure 7 presents the velocity vectors for the planar cavity with dimensions of $L/D = 1$ and 6. These calculations were performed using the standard k-ε RANS model. As with axisymmetric cavities, flow separation occurs at the sharp corner of the forebody. The streamwise pressure gradient increases until the flow reattaches at the sharp corner of the afterbody for $L/D = 1$ and impinges on the afterbody for $L/D = 6$. For the latter case, the flow momentum is not sufficient, hence flow impingement occurs. For $L/D = 1$, a corotating vortex is seen inside the cavity with its center nearly at the center of the cavity. Thereby, this configuration resembles that of $x/D_o = 0.5$ (shown in Fig. 3). We, consequently, state that the flow is in the SCV regime. Nonetheless, at $L/D = 6$, the vortex is elongated and characterized by flow impingement, exhibiting similarities to that corresponding to $x/D_o = 0.7$ (shown in Fig. 3). Thus, this flow corresponds to the CCV regime. Furthermore, these results plainly suggest that there is a critical cavity length to depth ratio L/D, at which a single vortex does no longer fit in the cavity. For instance, Zdanski et al. [12] showed that, for a trench cavity like this one, vortex encapsulation takes place at $L/D \sim 6.65$. Recall from the previous section that vortex encapsulation refers to two vortices in the cavity without inside-cavity flow reattachment.

Figure 8 presents the change on drag ΔC_D as a function of cavity length to depth ratio L/D. The individual contributions of pressure $\Delta C_{D,P}$ and shear $\Delta C_{D,S}$ drag are also plotted. Both pressure and shear drag increases with increasing L/D. $\Delta C_{D,P}$ increases due to flow impingement on the afterbody wall, as suggested by Fig. 7. It is obvious that shear drag is negligible for both axisymmetric and planar cavities. In comparison with Fig. 4, it is interesting to note that, for our planar cavity, there is no absolute minimum $\Delta C_{D,P}$. This is, however, expected because we modified the cavity to avoid flows in the WBF and UCV regimes. It is evident that, by increasing L/D, the flow transitions from the SCV to the CCV regime. This also suggests that the vortex for the range of L/D studied here exhibits characteristics of forced vortices (i.e., $n = 2$ and the pressure increases almost quadratically with increasing vortex radius). Now it is

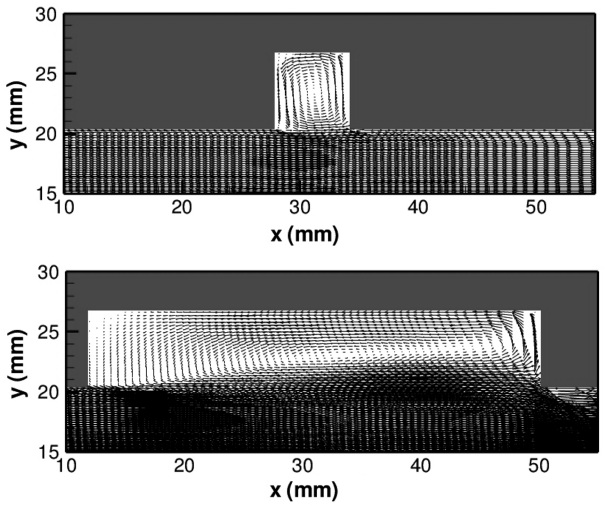

Fig. 7 Velocity vectors for the planar cavity with dimensions of $L/D = 1$ and 6. The calculations were performed using the standard k-ε RANS model.

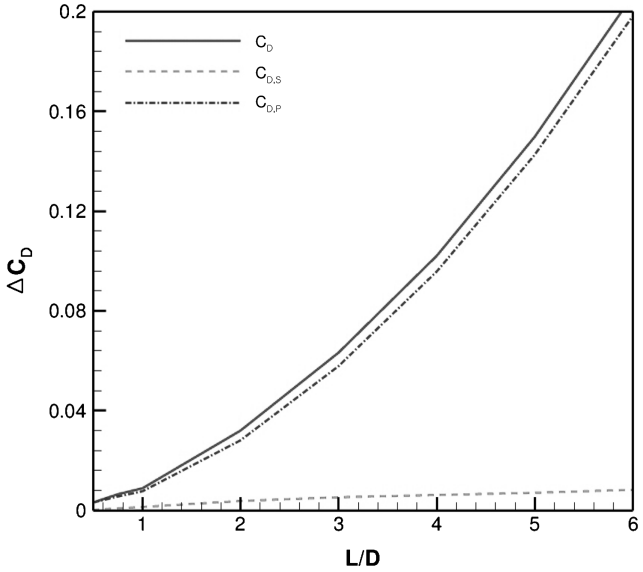

Fig. 8 Change in drag coefficient ΔC_D as function of cavity length to depth ratio L/D. The individual contributions of pressure $\Delta C_{D,P}$ and shear $\Delta C_{D,S}$ drag are also plotted.

important to examine the pressure distribution on the forebody and afterbody walls.

Figure 9 presents the pressure coefficient C_P as function of vertical distance y at the forebody (solid) and afterbody (dashed) walls. For $L/D = 1$, the absolute minimum C_P occurs at the center of the forebody and afterbody walls, indicating that the vortex center is located at the cavity center. Both C_p profiles and magnitudes in the forebody and afterbody walls are very similar, indicating that the horizontal forces are nearly balanced, exhibiting minimum flow oscillations. With increasing length to depth ratio L/D, C_P on the afterbody wall increases, whereas that on the forebody wall decreases. Because both C_p profiles and magnitudes in the forebody and afterbody walls are very different, horizontal forces are not balanced and the flow would exhibit large oscillations. The location of the absolute minimum C_P on the afterbody wall is shifted inward due to flow impingement on the afterbody wall. Note that this shift is consistent with that observed for $x/D_o = 0.6$ and 0.7 in Fig. 5.

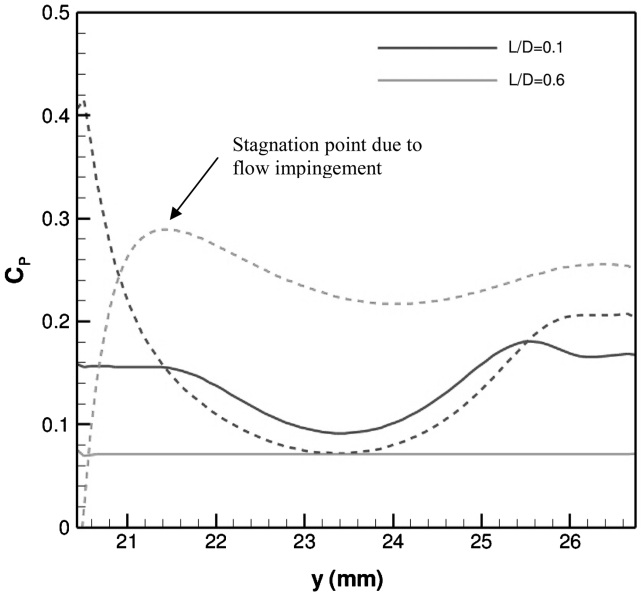

Fig. 9 Pressure coefficient C_P as function of vertical distance y at the forebody (solid) and afterbody (dashed) walls. The calculations were performed using the standard k-ε RANS model. The location of the stagnation point due to flow impingement is also indicated.

This again confirms qualitative similarities between that flow configuration in the axisymmetric cavity with afterbody disk at $x/D_o = 0.7$ and the flow in the planar cavity with $L/D = 6$.

DNS calculations were performed for the cavity sizes discussed in the context of Fig. 9 and the change in pressure drag $\Delta C_{D,P}$ as a function of dimensionless time τ^* is presented in Fig. 10. Whereas the RANS simulation provided steady values of $\Delta C_{D,P}$, the DNS provides unsteady values of $\Delta C_{D,P}$. Nevertheless, similar to the results of Fig. 8, the DNS results indicate that with increasing L/D, $\Delta C_{D,P}$ increases. Note that, for $L/D = 1.0$, the average $\Delta C_{D,P}$ is nearly 0.0 consistent with the result in Fig. 8. However, when $L/D = 6.0$, the average $\Delta C_{D,P}$ is $\sim$0.7, which is several times larger than that of Fig. 8. DNS and RANS simulations provide qualitative results; however, they might differ on their quantitative results.

D. Effect of Fuel and Air Injections on Flow Unsteadiness in Small Planar Cavities

This section is concerned with the pressure drag and flow characteristics in the small planar cavity due to fuel and air injection configurations. The schematic of normal injection (NI) and reverse injection (RI) configurations for air jets is presented in Fig. 11. In this figure, three possible fuel jet injection configurations are also depicted: coflow, crossflow, and counterflow with respect to the mainstream flow. As discussed in the Introduction, NI with crossflow corresponds to config. 1 examined by Zelina et al. [3]. The temporal pressure drag evolution for the configurations discussed in the context of Fig. 11 is presented in Fig. 12. For the NI of air jets, pressure drag oscillations start to fluctuate after a finite time of $\sim$0.4 ms, whereas for RI, pressure drag fluctuations start immediately as the simulation starts. This suggests that flow disturbances propagate faster when RI is used. For NI, the crossflow-fuel-jet position exhibits the lowest pressure drag amplitudes, followed very closely by the coflow fuel jet position. The counterflow fuel jet position, on the other hand, exhibits the highest pressure drag amplitudes. Recall from Secs. III.B and III.C that the optimum flow configuration that leads to lowest flow unsteadiness is that of the SCV regime, which contains a corotating forcedlike vortex with the mainstream with minimum flow impingement on the afterbody wall. Therefore, when the fuel jet is injected in counterflow with respect to the mainstream, the corotating vortex existing in the cavity is distorted. On the contrary, when fuel jet is injected in crossflow or coflow, the corotating vortex is not distorted and possibly enhanced. This explains why the crossflow and coflow fuel-injection positions exhibit superior flow steadiness with respect to the counterflow fuel-injection position. Moreover, RI promotes a counter-rotating cavity

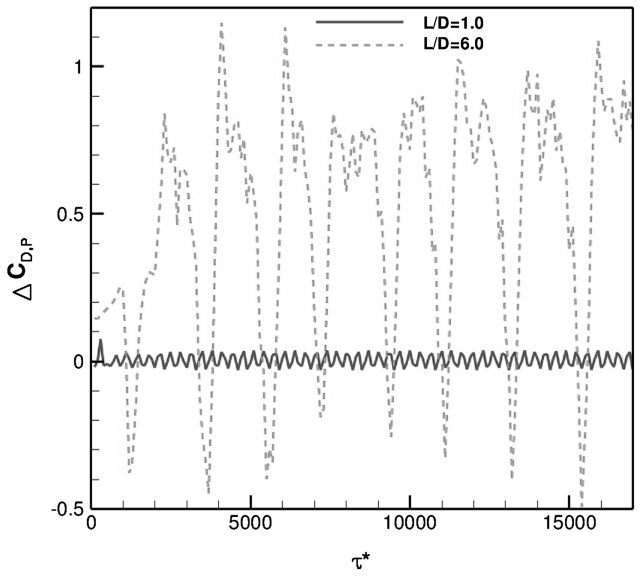

Fig. 10 Change in pressure drag $\Delta C_{D,P}$ as a function of dimensionless time τ^*. The calculations were performed using DNS.

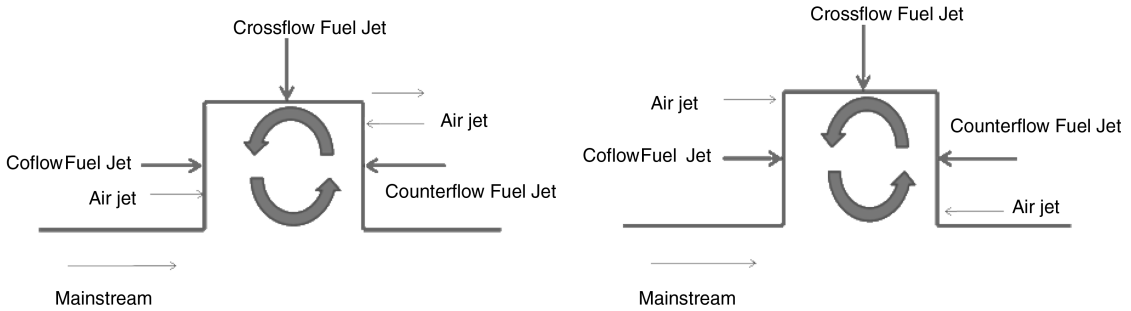

Fig. 11 Schematic of the a) normal injection and b) reverse injection configuration of air jets. The multiple positions of fuel jets are also indicated.

vortex (with respect to the mainstream flow). This in turn increases the flow unsteadiness as demonstrated by the larger pressure drag amplitudes. The flow in the RI is nearly insensitive to the fuel-jet injection positions. Counterflow-fuel-jet position and RI provide the worst-case scenario in terms of flow unsteadiness.

E. Effect of Cavity Equivalence Ratio and Combustion to Flame/Flow Unsteadiness

This section is concerned with the pressure drag and flow/flame characteristics in the small planar cavity due to combustion under various cavity equivalence ratios ϕ_{CAV}. The cavity equivalence ratios ϕ_{CAV} used are 0.85, 1.42, 2.15, 5.67, 8.5, and 11.33. As ϕ_{CAV} is increased, the cavity air to fuel jet momentum ratio λ_{CAV} decreases from 9.9 to 5.85, 3.87, 1.47, 0.97, and 0.74, respectively. The velocity in the main stream is equaled to the velocity of the air jets to reduce the effect of shear between the air mainstream flow and the outermost air jet. The mainstream temperature is constant at 533 K and its profile is uniform. The cavity walls are assumed isothermal at 533 K. A total number of 12 simulations were run corresponding to the six ϕ_{CAV} and two injection configurations for the air jets (cf. Figure 11). The fuel jet is injected in crossflow with the respect to the mainstream air flow. The instantaneous temperature contours, streamlines (lines), and streak lines (dots) for $\phi_{\mathrm{CAV}} = 2.15, 5.67, 8.5$, and 11.33 using NI and RI are presented in Fig. 13. The streamlines are computed from the fuel and air jets, whereas the streak lines are computed from the fuel jet only. These streak lines, in fact, represent massless particles injected through the fuel jet. Temperature contours and streamlines reveal that, when NI is used, two nonpremixed flames attached to the air jet ports are formed. On the other hand, the nonpremixed flames are attached to the fuel jet and the counterflow air jet ports when RI is used. A plausible explanation is that, if the flame were to be attached to the coflow air jet port, the curvature-induced stretch would be high enough to extinguish the flame. Consequently, the flames established in the NI configuration appeared to be more parallel to the mainstream than the flames in the RI configuration. With NI, the particles are accumulated toward the forebody face of the cavity. On the contrary, particles are clustered toward the afterbody face of the cavity when RI is used. This plainly indicates that fuel is transported toward the forebody face of the cavity and afterbody face of the cavity when NI and RI are used, respectively. Moreover, this fact is consistent with the relatively high temperature encountered in the forward and backward cavity regions for the NI and RI, respectively. Qualitatively, it appears that, regardless of ϕ_{CAV}, it is more difficult for particles to escape the cavity when RI is used. This is because the particles have to go against the flow when they are still in the cavity as illustrated by the streamlines and streak lines.

Figure 14 shows the temporal temperature profiles for the NI (solid) and RI (dashed) for the conditions discussed in the context of Fig. 13. The temperatures are probed at $x = 34$ mm and $y = 22$ mm (cf. Figs. 3 and 13). Note that, at $\phi_{\mathrm{CAV}} = 0.85, 1.42, 2.15, 5.67, 8.5$, and 11.33, the temperature starts increasing and/or oscillating at $\sim$1.5, 0.5, 0.25, 0.11, 0.09, and 0.19 ms, respectively, for the NI case. For ease of discussion, we refer to this time as the ignition time. It is reasonable to qualitatively observe that the mixture ignition time is the slowest at off-stoichiometric conditions (i.e., $\phi_{\mathrm{CAV}} = 8.5$ and 11.33). The ignition time is, however, not the lowest at $\phi_{\mathrm{CAV}} = 1.42$ because the chemistry model used in this investigation does not account for CO_2 and H_2O dissociation. Therefore, these results can only be interpreted qualitatively. The ignition time for RI is always larger than for their NI counterparts. This is a reasonable result because the large pressure drag fluctuations observed in Fig. 12 for RI would tend to inhibit ignition. For low ϕ_{CAV}, the amplitude of the temperature fluctuations is larger for RI than it is for NI. Nevertheless, as ϕ_{CAV} increases, the amplitude and frequency of temperature oscillations decrease for RI, whereas those for NI

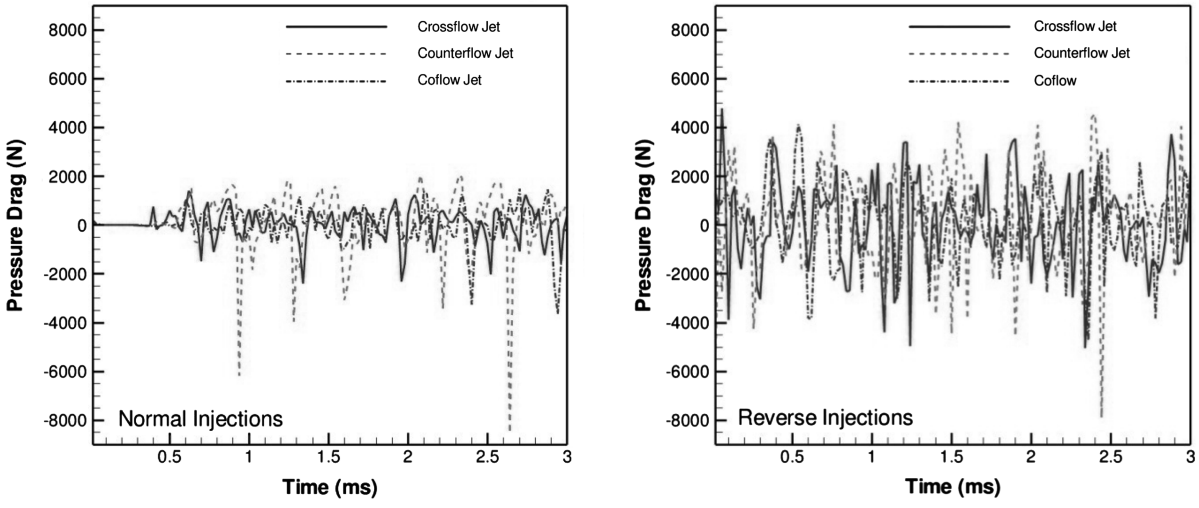

Fig. 12 Pressure drag as a function of time for the normal and reverse injection configurations. DNS were performed for these calculations.

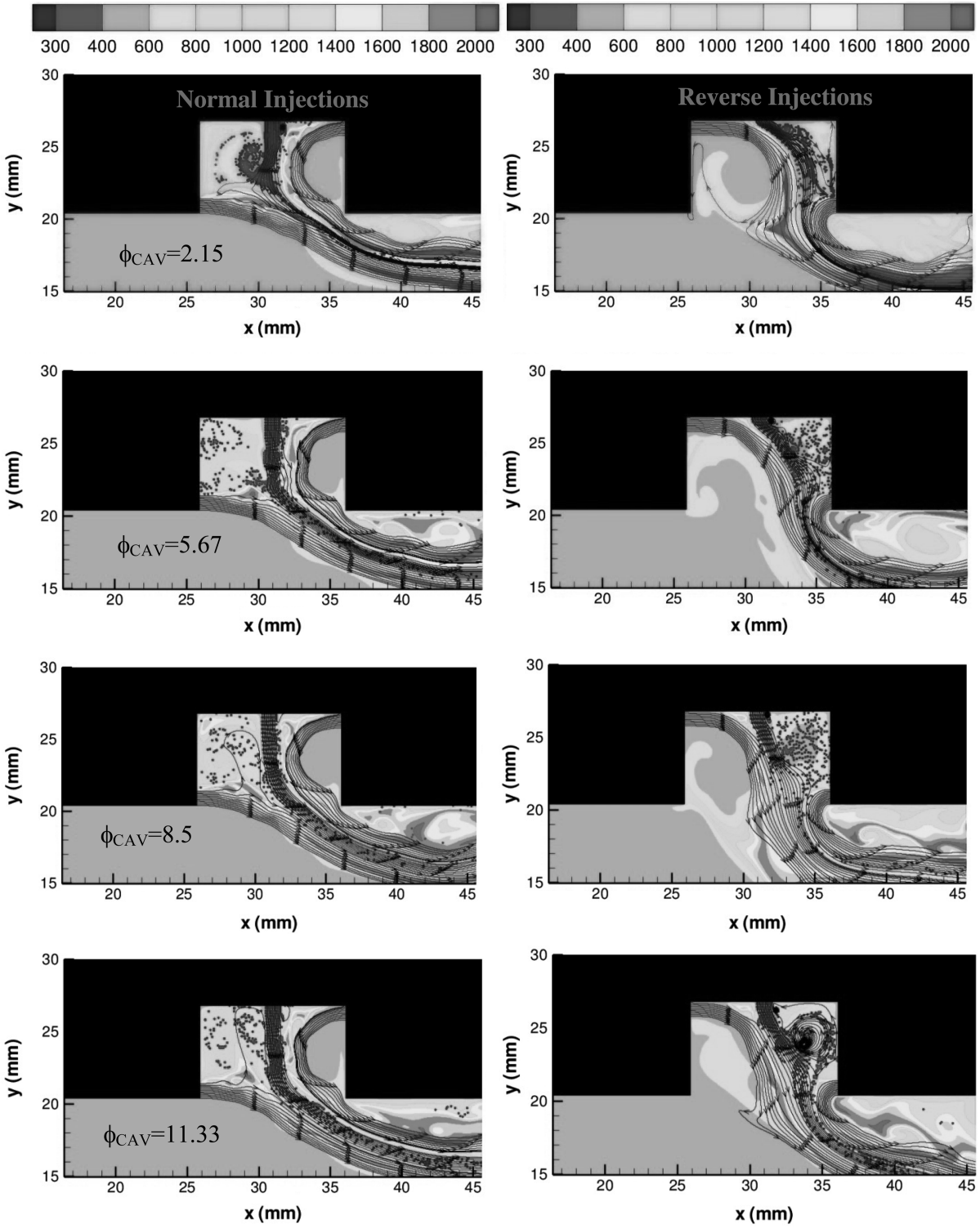

Fig. 13 Instantaneous temperature contours, velocity streamlines (lines), and streak lines (dots) after 3 ms for cavity equivalence ratios ϕ_{CAV} of 2.15, 5.67, 8.5, and 11.33 under NI (left) and RI (right) configurations.

generally increase. However, the effect of ϕ_{CAV} appears to be more pronounced for RI. So, at high ϕ_{CAV}, the amplitude and frequency of the temperature fluctuations is larger for NI than it is for RI.

To further examine the effect of ϕ_{CAV} on flow unsteadiness, Fig. 15 presents the pressure drag as a function of time for relatively low and high ϕ_{CAV} (i.e., 2.15 and 8.5). It is evident from Figs. 14 and 15 that, at low ϕ_{CAV}, flow unsteadiness is more pronounced for NI; nonetheless, at high ϕ_{CAV}, the flow unsteadiness for NI and RI become comparable. A possible explanation can be mentally visualized as follows:

1) For NI conditions, as $\phi_{\mathrm{CAV}} \to 0$ $\lambda_{\mathrm{CAV}} \to \infty$, and the effect of the fuel jet on the air jets becomes negligible. Consequently, we would expect a flow structure resembling that of an axisymmetric cavity with afterbody disk at $x/D_o = 0.5$ (cf. Figure 3) or that of a planar cavity with $L/D = 1.0$ (cf. Figure 7) (i.e., steady cavity vortex). Therefore, low ϕ_{CAV} leads to low flow unsteadiness.

2) For NI, as $\phi_{\mathrm{CAV}} \to \infty$ $\lambda_{\mathrm{CAV}} \to 0$, and the effect of the fuel jet on the air jets becomes significant. The previously established structure becomes distorted and the flow unsteadiness increases. Therefore, high ϕ_{CAV} leads to high flow unsteadiness. This is consistent

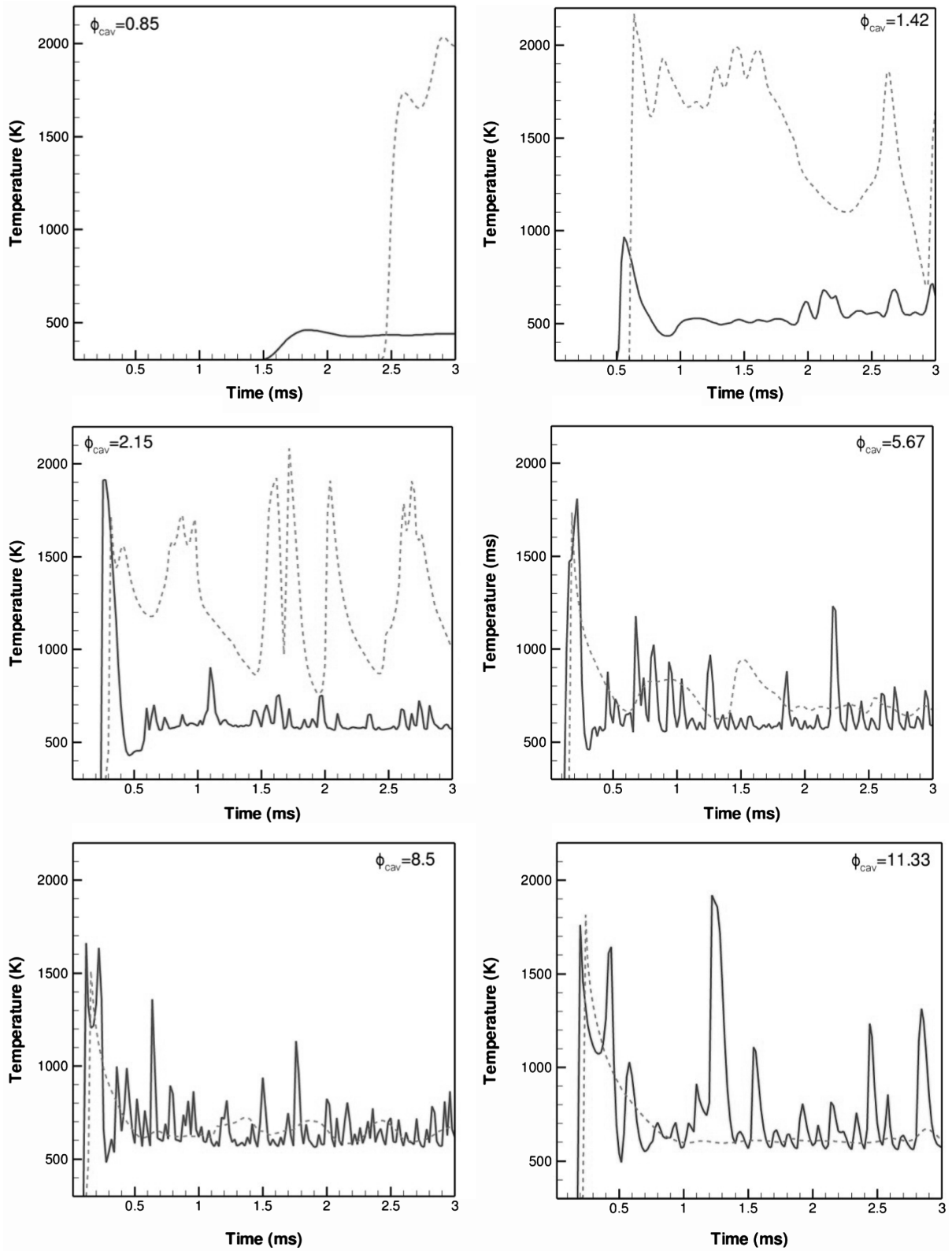

Fig. 14 Temporal temperature profiles for the normal (solid) and reverse (dashed) Injections. The simulations were performed using DNS. The temperatures are probed at $x = 34$ mm and $y = 22$ mm (cf. Figs. 3 and 13).

with Zelina et al. [3] who showed, as discussed in the Introduction, that decreasing λ_{CAV} leads to higher ϕ_{CAV} at lean blowout for NI of air and crossflow fuel injection. Because near-extinction conditions are associated with flow oscillations [32], the higher ϕ_{CAV} at lean blowout is interpreted here as higher flow unsteadiness. Nevertheless, blowout was not observed for any of our simulations because the global chemistry does not include elementary reactions needed for the correct assessment of flame extinction [33].

3) For RI conditions, as $\phi_{\mathrm{CAV}} \to \infty$ $\lambda_{\mathrm{CAV}} \to 0$, and the effect of the fuel jet on the air jets becomes negligible. Consequently, the flow inside the cavity resembles that presented for axisymmetric cavity with afterbody disk at $x/D_o = 0.2$ (cf. Figure 3) (i.e., wake backflow). Therefore, high ϕ_{CAV} leads to high flow unsteadiness.

4) For RI, as $\phi_{\mathrm{CAV}} \to 0$ $\lambda_{\mathrm{CAV}} \to \infty$, and the effect of the fuel jet on the air jets becomes significant. The previously established structure becomes distorted and the flow unsteadiness decreases.

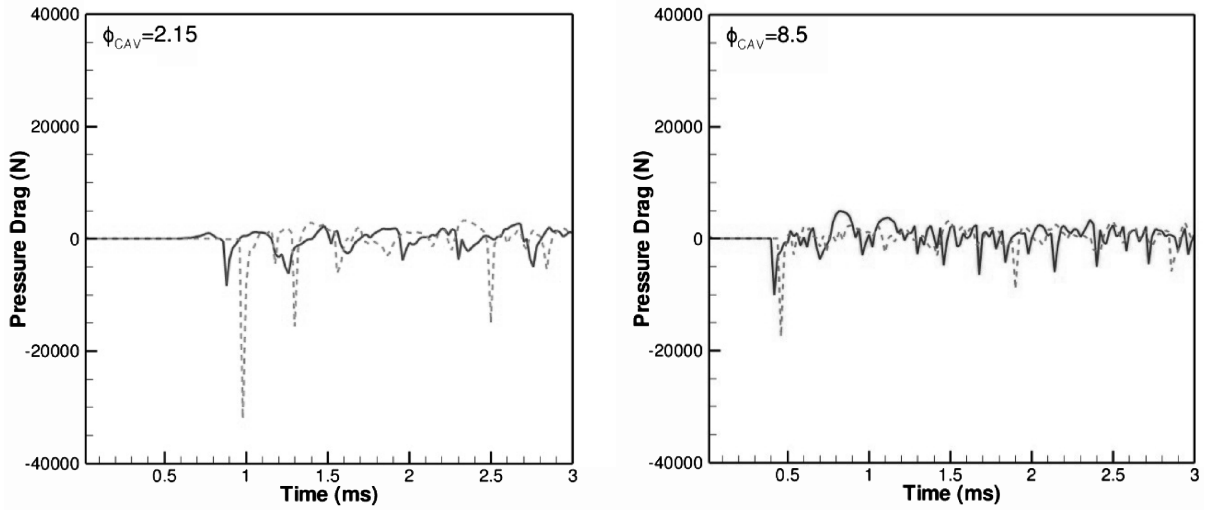

Fig. 15 Pressure drag as a function of time for cavity equivalence ratio ϕ_{CAV} of 2.15 and 8.5. The simulations were performed using DNS. Normal and reverse injections are indicated in solid and dashed lines, respectively.

IV. Conclusions

An extensive computational investigation on the characteristics of cavity-stabilized flames was presented. We examined the flow unsteadiness in both axisymmetric and (nonreactive and reactive flow past) planar cavities. Important conclusions are as follows:

1) Results indicate that shear drag coefficient $\Delta C_{D,S}$ is negligible in comparison with pressure drag coefficient $\Delta C_{D,P}$, and the former is proportional to flow unsteadiness.

2) The axisymmetric cavity, which consists of a forebody and an afterbody disk, exhibits multiple flow regimes depending on the distance between the forebody and afterbody disk. When the distance between the forebody and afterbody disk x/D_o is small, multiple vortices are formed in the cavity. However, it contains a main counter-rotating freelike vortex with respect to the mainstream flow that is formed due to the backflow (wake backflow regime). As with previous investigations on axisymmetric cavities, results indicate that with increasing cavity length the drag decreases as the flow transitions to the unsteady cavity vortex regime, characterized by backflow and flow contraction around the afterbody disk. Further increase on cavity length reduces the drag to an absolute minimum as the flow transitions to the steady cavity vortex regime. This regime is characterized by a corotating forcedlike vortex with neither backflow nor mainstream flow impingement. With further increase in x/D_o, the drag increases again as the flow transitions to the compressed cavity vortex regime, characterized by an elongated corotating forcedlike vortex with mainstream flow impingement on the afterbody disk.

3) Results indicate that with increasing planar cavity length the pressure drag increases monotonically as the flow in the cavity transitions from SCV to CCV regime. The vortex formed in the cavity exhibits forced-vortex pressure profiles as those present in the axisymmetric cavities. The planar cavity does not exhibit characteristics of the WBF and UCV regimes due to two reasons: 1) the forebody and afterbody depth D are equal, and 2) the afterbody thickness for the planar cavity is infinitely long in comparison with that of the axisymmetric cavity.

4) Normal injections (i.e., the outermost air jet is in coflow with the air mainstream flow, and the innermost air jet is in counterflow) present superior flow steadiness characteristics than their reverse injection counterpart (i.e., the outermost jet is in counterflow with the air mainstream flow and the innermost air jet is in coflow). This is because RI promotes counter-rotating vortex formation, resembling WBF. In the NI, the crossflow fuel jet promotes superior flow steadiness than the counterflow fuel jet. Crossflow-fuel-jet injection is slightly better in terms of flow steadiness than the coflow fuel jet injection. However, with RI, the three fuel jet injection positions (crossflow, coflow, and counterflow) exhibit comparable flow unsteadiness.

5) Cavity-stabilized flames were established at various cavity equivalence ratios ϕ_{CAV} under NI and RI. For NI, low ϕ_{CAV} (with high air to fuel momentum ratio λ_{CAV}) leads to low flow unsteadiness because the air jets promote corotating vortex formation in the cavity. At high ϕ_{CAV} (low λ_{CAV}), on the other hand, the fuel jet distorts the corotating vortex; hence, flow unsteadiness increase. For RI, low ϕ_{CAV} leads to high flow unsteadiness because the air jets promote counter-rotating vortex formation in the cavity. On the contrary, at high ϕ_{CAV}, the fuel jet distorts the formation of corotating vortex(es), increasing flow steadiness.

6) The results presented in this investigation suggest that, for minimizing cavity flow unsteadiness, designers need to focus on geometric dimensions, and fuel/air injection positioning and ϕ_{CAV} that promote corotating forcedlike vortex formation, and reduce both backflow and flow mainstream impingement on the afterbody wall.

Acknowledgments

This material is based on research sponsored by U.S. Air Force Research Laboratory under agreement number F33615-03-2-2347. We also thank W. M. Roquemore from the U.S. Air Force Research Laboratory/RZTC for his insightful comments. The views and conclusions contained herein are those of the authors and should not be interpreted as necessarily representing the official policies or endorsements, either expressed or implied, of U.S. Air Force Research Laboratory or the U.S. Government.

References

[1] Zelina, J., Sturgess, G. J., and Shouse, D. T., "The Behavior of an Ultra-Ccompact Combustor (UCC) Based on Centrifugally-Enhanced Turbulent Burning Rates," *40th AIAA/ASME/SAE/ASEE Joint Propulsion Conference and Exhibit*, AIAA Paper 2004-3541, 2004.

[2] Greenwood, R. T., Anthenien, R. A., and Zelina, J., "Computational Analysis of the Ultra Compact Combustor," *43rd AIAA Aerospace Sciences Meeting and Exhibit*, AIAA Paper 2005-220, 2005.

[3] Zelina, J., Anderson, W., Koch, P., and Shouse, D. T., "Compact Combustion Systems Using a Combination of Trapped Vortex and High-g Combustor Technologies," *Proceedings of ASME Turbo Expo 2008: Power for Land, Sea, and Air*, American Society of Mechanical Engineers, GT2008-50090, 2008.

[4] Zelina, J., Ehret, J., Hancock, R. D., Shouse, D. T., and Roquemore, W. M., "Ultra-Compact Combustion Technology Using High Swirl for Enhanced Burning Rate," *38th AIAA/ASME/SAE/ASEE/ Joint Propulsion Conference & Exhibit*, AIAA Paper 2002-3725, 2002.

[5] Zelina, J., Sturgess, G. J., and Shouse, D. T., "The Behavior of an Ultra-Compact Combustor (UCC) Based on Centrifugally-Enhanced Turbulent Burning Rates," *40th AIAA/ASME/SAE/ASEE/ Joint Propulsion Conference & Exhibit*, AIAA Paper 2004-3541, 2004.

[6] Greenwood, R. T., Anthenien, R. A., and Zelina, J., "Computational Analysis of the Ultra Compact Combustor," *43th Aerospace Sciences*

Meeting & Exhibit, AIAA Paper 2005-220, 2005.

[7] Mawid, M. A., Park, T. W., Thornburg, H., Sekar, B., and Zelina, J., "Numerical Analysis of Inter-turbine Burner (ITB) Concepts for Improved Gas Turbine Engine Performance," *43th Aerospace Sciences Meeting & Exhibit*, AIAA Paper 2005-1162, 2005.

[8] Mair, W. R., The Effect of a Rear-mounted Disc on the Drag of a Blunt-based Body of Revolution, *The Aeronautical Quarterly*, Vol. 16, Pt. 4, Nov. 1965, pp. 350–360.

[9] Little, B. H., Jr., and Whipkey, R. R., "Locked Vortex Afterbodies," *Journal of Aircraft*, Vol. 16, No. 5, 1979, pp. 296–302. doi:10.2514/3.58522

[10] Katta, V. R., and Roquemore, W. M., "Numerical Studies on Trapped-Vortex Concepts for Stable Combustion," *Transactions of the ASME: Journal of Engineering for Gas Turbines and Power*, Vol. 120, No. 1, 1998, pp. 60–68. doi:10.1115/1.2818088

[11] Katta, V. R., and Roquemore, W. M., "Numerical Studies of Trapped-vortex Combustor," *32nd AIAA/ASME/SAE/ASEE/Joint Propulsion Conference & Exhibit*, AIAA Paper 1996-2660, 1996.

[12] Zdanski, P. S. B., Ortega, M. A., and Fico, N. G. C. R., Jr., "On the Flow over Cavities of Large Aspect Ratio: A Physical Analysis," *International Communications in Heat and Mass Transfer*, Vol. 33, No. 4, 2006, pp. 458–466. doi:10.1016/j.icheatmasstransfer.2006.01.007

[13] Zdanski, P. S. B., Ortega, M. A., and Fico, N. G. C. R., Jr., "Numerical Study of the Flow over Shallow Cavities," *Computers and Fluids*, Vol. 32, No. 7, 2003, pp. 953–974. doi:10.1016/S0045-7930(02)00067-1

[14] D'yanchenko, A. Y., Terekhov, V. I., and Yarygina, N. I., "Vortex Formation and Heat Transfer in Turbulent Flow Past a Transverse Cavity with Inclined Frontal and Rear Walls," *International Journal of Heat and Mass Transfer*, Vol. 51, Nos. 13–14, 2008, pp. 3275–3286. doi:10.1016/j.ijheatmasstransfer.2007.11.039

[15] Puranam, S., Arici, J., Sarzi-Amade, N., and Dunn-Rankin, D., Sirignano, "Turbulent Combustion in a Curving, Contracting Channel with a Cavity Stablized Flame," *Proceedings of the Combustion Institute*, Vol. 32, No. 2, 2009, pp. 2973–2981. doi:10.1016/j.proci.2008.06.161

[16] Katta, V. R., Zelina, J., and Roquemore, W. M., "Numerical Studies on Cavity-Inside-Cavity-Supported Flames in Ultra Compact Combustor," *Proceedings of the ASME Turbo Expo 2008: Power for Land, Sea, and Air*, American Society of Mechanical Engineers, GT2008-50853, 2008.

[17] Shu, Z., Aggarwal, S. K., Katta, V. R., and Puri, I. K., "Flame-Vortex Dynamics in an Inverse Partially Premixed Combustor: The Froude Number Effects," *Combustion and Flame*, Vol. 111, No. 4, 1997, pp. 276–286. doi:10.1016/S0010-2180(97)00018-7

[18] Azzoni, R., Ratti, S., Puri, I. K., and Aggarwal, S. K., "Gravity Effects on Triple Flames: Flame Structure and Flow Instability," *Physics of Fluids*, Vol. 11, No. 11, 1999, pp. 3449–3464. doi:10.1063/1.870203

[19] Qin, X., Puri, I. K., Aggarwal, S. K., and Katta, V. R., "Gravity, Radiation and Coflow Effects on Partially Premixed Flames," *Physics of Fluids*, Vol. 16, No. 8, 2004, pp. 2963–2974. doi:10.1063/1.1764835

[20] Siegel, R., and Howell, J. R., *Thermal Radiation Heat Transfer*, Hemisphere, New York, 1981.

[21] Lee, B. J., and Chung, S. H., "Stabilization of Lifted Tribrachial Flames in a Laminar Nonpremixed Flame," *Combustion and Flame*, Vol. 109, Nos. 1–2, 1997, pp. 163–172. doi:10.1016/S0010-2180(96)00145-9

[22] Katta, V. R., Goss, L. P., and Roquemore, W. M., "Numerical Investigations of Transitional H_2/N_2 Jet Diffusion Flames," *AIAA Journal*, Vol. 32, No. 1, 1994, pp. 84–94. doi:10.2514/3.11954

[23] Bird, R. B., Stewart, W. E., and Lightfoot, E. N., *Transport Phenomena*, Wiley, New York, 1960.

[24] Reid, R. C., Prausnitz, J. M., and Poling, B. E., *The Properties of Gases and Liquids*, McGraw–Hill, New York, 1987.

[25] Chu, W.-W., Yang, V., and Majdalani, J., "Premixed Flame Response to Acoustic Waves in a Porous-Walled Chamber with Surface Mass Injection," *Combustion and Flame*, Vol. 133, No. 3, 2003, pp. 359–370. doi:10.1016/S0010-2180(03)00018-X

[26] "Ansys Fluent 12.0 Theory Guide," Ansys, Ann Arbor, MI, www.fluent.com.

[27] Kee, R. J., Rupley, F. M., Miller, J. A., Coltrin, M. E., Grcar, J. F., Meeks, E., Moffat, H. K., Lutz, A. E., Dixon-Lewis, G., Smooke, M. D., et al., "Chemkin Release 4.1.1," Reaction Design, San Diego, CA, 2007.

[28] Katta, V. R., Mawid, M., Sekar, B., Corporan, E., and Montgomery, C. J., "Comparison of Chemical-Kinetics Models for JP-8 Fuels in Predicting Premixed and Nonpremixed Flames," *42nd AIAA/ASME/ASEE Joint Propulsion Conference and Exhibit*, AIAA Paper 2006-4745, 2006.

[29] Katta, V. R., Meyer, T. R., Brown, M. S., Gord, J. R., and Roquemore, W. M., "Extinction Criterion for Unsteady, Opposing-Jet Diffusion Flames," *Combustion and Flame*, Vol. 137, Nos. 1–2, 2004, pp. 198–221. doi:10.1016/j.combustflame.2004.02.004

[30] Grisch, F., Attal-Tretout, B., Bresson, A., Bouchardy, P., Katta, V. R., and Roquemore, W. M., "Investigation of a Dynamic Diffusion of H_2 in Air with Laser Diagnostics and Numerical Modeling," *Combustion and Flame*, Vol. 139, Nos. 1–2, 2004, pp. 28–38. doi:10.1016/j.combustflame.2004.08.002

[31] Gharib, M., and Roshko, A., "The Effect of Flow Oscillations on Cavity Drag," *Journal of Fluid Mechanics*, Vol. 177, April 1987, pp. 501–530. doi:10.1017/S002211208700106X

[32] Füri, M., Papas, M., and Monkewitz, P. A., "Non-Premixed Jet Flame Pulsations Near Extinction," *Proceedings of the Combustion Institute*, Vol. 28, Pt. 1, 2000, pp. 831–838.

[33] Takahashi, F., and Katta, V. R., "A Reaction Kernel Hypothesis for the Stability Limit of Methane Jet Diffusion Flames," *Proceedings of the Combustion Institute*, Vol. 28, Pt. 2, 2000, pp. 2071–2078.

T. Jackson
Associate Editor